Nano Research 2018, 11(1): 554–564
https://doi.org/10.1007/s12274-017-1712-2
Research Article
ISSN 1998-0124
CN 11-5974/O4

Highly-anisotropic optical and electrical properties in layered SnSe

Shengxue Yang[1,2,§] (✉), Yuan Liu[3,§], Minghui Wu[4,§], Li-Dong Zhao[2], Zhaoyang Lin[1], Hung-chieh Cheng[3], Yiliu Wang[1], Chengbao Jiang[2], Su-Huai Wei[5], Li Huang[4], Yu Huang[3,6], and Xiangfeng Duan[1,6] (✉)

[1] *Department of Chemistry and Biochemistry, University of California, Los Angeles, CA 90095, USA*
[2] *School of Materials Science and Engineering, Beihang University, Beijing 100191, China*
[3] *Department of Materials Science and Engineering, University of California, Los Angeles, CA 90095, USA*
[4] *Department of Physics, South University of Science and Technology of China, Shenzhen 518005, China*
[5] *Beijing Computational Science Research Center, Beijing 100094, China*
[6] *California Nanosystems Institute, University of California, Los Angeles, CA 90095, USA*
[§] *Shengxue Yang, Yuan Liu, and Minghui Wu contributed equally to this work.*

Received: 29 March 2017
Revised: 8 June 2017
Accepted: 10 June 2017

KEYWORDS
layered SnSe,
anisotropy,
angle-resolved transports,
polarized Raman scattering,
angle-resolved optical absorption

ABSTRACT

Anisotropic materials are of considerable interest because of their unique combination of polarization- or direction-dependent electrical, optical, and thermoelectric properties. Low-symmetry two-dimensional (2D) materials formed by van der Waals stacking of covalently bonded atomic layers are inherently anisotropic. Layered SnSe exhibits a low degree of lattice symmetry, with a distorted NaCl structure and an in-plane anisotropy. Here we report a systematic study of the in-plane anisotropic properties in layered SnSe, using angle-resolved Raman scattering, optical absorption, and electrical transport studies. The optical and electrical characterization was direction-dependent, and successfully identified the crystalline orientation in the layered SnSe. Furthermore, the dependence of Raman-intensity anisotropy on the SnSe flake thickness and the excitation wavelength were investigated by both experiments and theoretical calculations. Finally, the electrical transport studies demonstrated that few-layer SnSe field-effect transistors (FETs) have a large anisotropic ratio of carrier mobility (~ 5.8) between the armchair and zigzag directions, which is a record high value reported for 2D anisotropic materials. The highly-anisotropic properties of layered SnSe indicate considerable promise for anisotropic optics, electronics, and optoelectronics.

1 Introduction

Two-dimensional (2D) layered materials have attracted considerable interest for their unique layer-number-dependent physical, chemical, and optical properties, and have potential application in diverse fields [1].

Address correspondence to Shengxue Yang, sxyang@buaa.edu.cn; Xiangfeng Duan, xduan@chem.ucla.edu

Generally, the lattice structure and symmetry of 2D materials are essential for determining their fundamental properties. Graphene and most of the well-studied 2D transition metal dichalcogenides (TMDs) with high lattice symmetry exhibit isotropic in-plane behavior; however, it has been reported that a few low-symmetry 2D materials have anisotropic in-plane optical, electrical, mechanical and thermal properties [1–3]. Defined by their structure, anisotropic 2D materials can be divided into two categories: The first consists of those with an unique disordered 1T structure, such as ReS_2, $ReSe_2$, and WTe_2 [4–9]; in contrast, members of the second possess a puckered honeycomb structure, and typical materials are black phosphorus (BP), SnSe, GaSe, GaTe, and SnTe [10–16].

The unique angle-dependent properties of such anisotropic 2D materials allow for designing new electronic and optoelectronic devices that cannot be easily realized in isotropic materials [17–20]. For example, anisotropy in low-symmetry 2D materials can be exploited to develop mid-infrared polarizers, polarization sensors, artificial synaptic devices, and 2D logic circuits [1, 8, 18, 21]. Furthermore, the crystalline orientation in anisotropic 2D materials can be used in a variety of device designs, for example, aligning field-effect transistors (FETs) in a particular direction to tune their transport properties and optimize performance, and fabricating high-performance photodetectors [19]. By using a particular crystalline orientation, a large and non-saturating magnetoresistance has been achieved in anisotropic 2D materials, which suggests significant potential as magnetic sensors [8]. Therefore, investigation of anisotropic properties dependent on crystalline orientation is of considerable interest.

Tin selenide (SnSe) is an important narrow-bandgap semiconductor with a low-symmetry crystal structure [11, 22–28]. Bulk SnSe crystal exhibits strongly anisotropic thermoelectric properties, namely, that a high maximum thermoelectric figure of merit (designated ZT) at 923 K can be realized along the *b*-axis (2.6 ± 0.3), but has a significantly reduced value (0.8 ± 0.2) along the *a*-axis [23]. Meanwhile, there are promising applications of SnSe in various electronic and optoelectronic fields, such as solar cells [24], infrared optoelectronic devices [25], radiation detectors [26], electrical switching and polarity-dependent memory switching devices [27], and spin-transport devices [28]. By comparison with its bulk counterpart, 2D SnSe is expected to possess a tunable band gap, a large absorption coefficient, and a high photosensitivity [25, 29] as a result of the large surface-to-volume ratio and quantum confinement effects [22]. Because of its layered structure, atomically-thin SnSe may be produced by mechanical exfoliation from bulk SnSe or by chemical vapor deposition [29]. To date, the exploration of anisotropic properties in 2D SnSe has mainly focused on theoretical calculations [28, 30], while the direction-dependent electron, phonon, and photon interactions and related mechanisms, as well as the facile experimental identification of crystalline orientation, remain largely unexplored.

Here we report a systematic investigation of the in-plane anisotropy of the low-symmetry layered SnSe using polarization-dependent Raman scattering, optical absorption, and crystalline orientation-dependent electrical transport characteristics. In general, the anisotropic Raman intensity is strongly dependent on the SnSe flake thickness, and the optical absorption exhibits strong anisotropic behavior in the visible range. Furthermore, we observe a large anisotropic ratio of carrier mobility between two crystalline orientations owing to its unique anisotropic electron effective mass, which is the highest reported among 2D anisotropic materials to date. Our results not only reveal an anisotropic nature in the optical and electrical properties of layered SnSe, but also open a new pathway to identify the crystalline orientation, which is of great significance for the selective design of anisotropic layered SnSe-based electronic and optoelectronic devices.

2 Experimental section

2.1 Sample and device preparation

SnSe crystals were grown by the Bridgman crystal growth method [23]. Layered SnSe flakes were isolated from a bulk SnSe single crystal by micromechanical exfoliation onto 300 nm $SiO_2/p^{++}Si$ and quartz substrates; the thicknesses of the SnSe flakes were determined by atomic force microscopy (AFM) (Bruker Dimension

Icon Scanning Probe Microscope). For the transmission electron microscopy (TEM) measurement, the SnSe flakes were first exfoliated onto a polyvinyl alcohol (PVA) film on the SiO_2/Si substrate, and the SnSe/PVA film was then transferred onto the TEM grid. Afterwards, the PVA film was removed by using chloroform. The TEM and selected-area electron diffraction (SAED) images were obtained using a Titan S/TEM FEI with an acceleration voltage of 300 kV. The FET devices of few-layer SnSe flakes were fabricated using standard electron-beam lithography followed by electron beam evaporation of 20 nm Ni and 50 nm Au.

2.2 Raman spectra measurement

Raman spectroscopy was performed using a Horiba LabRam HR800 system, with excitation wavelengths of 488 and 633 nm. Raman spectra were collected using a 100× objective and recorded with an 1,800 lines·mm^{-1} grating, providing a spectral resolution of ~ 1 cm^{-1}. The spot size of the laser was approximately 1 μm. The spectra were recorded at low power levels (P = 0.5 mW for the 633 nm laser and 1 mW for the 488 nm laser) to avoid laser-induced heating and ablation of the samples. For the angle-resolved Raman spectra measurements, the samples were placed on a rotation stage, and a parallel-backscattering configuration was used in which the polarizations of the incident and scattered light are parallel. The Raman intensity parameters were obtained by fitting the spectral peaks with a Lorentzian/Gaussian function.

2.3 Absorption characterization

The absorption spectra of SnSe flakes on the quartz substrate were measured using a lab-built absorption setup operating in the light transmission mode. The white light was generated using a laser driven light source (V-LUX 1000). For angle-resolved absorption measurements, the incident white light was linearly polarized (OLYMPUS U-POT polarizer) and the quartz substrate with SnSe flakes was placed on a rotation stage. The transmitted light was collected by the objective lens (50×, numerical aperture = 0.5) of an upright microscope and analyzed by a spectrometer (Princeton Instruments SpectraPro 2300i) with a CCD camera (Princeton Instruments CCD Model: 7509-001).

2.4 Theoretical calculations

The band structures of four SnSe flakes with different assumed thicknesses (bulk, monolayer, double-layer, and three-layer) were modeled by density-functional theory (DFT) using the projector augmented wave (PAW) method, implemented in VASP. As the commonly-used generalized gradient approach (GGA)-Perdew–Burke–Ernzerhof (PBE) approximation always lowers the band gap, we used the HSE06 hybrid function method to correct the band gap. The energy cutoff was set to 400 eV, and the K-point mesh to 11×11×4 for bulk SnSe, 11×11×1 for layered SnSe. All the structures considered were relaxed to atomic force levels less than 0.5 meV·Å^{-1}. The band symmetry is determined by the wave function of some k-point of the band. The spin-orbital interaction was also considered but was determined to have negligible effect on our results.

3 Results and discussion

SnSe is a representative layered IV–VI chalcogenide with orthorhombic crystal structure, which is composed of tightly-bonded double layers of Sn and Se atoms, as shown in Figs. 1(a) and 1(b). The symmetry group of its crystal structure is *Pnma*(62), which is formed by a severely distorted NaCl arrangement [22]. The x- and z-axes in Figs. 1(a) and 1(b) correspond to the in-plane armchair and zigzag directions, and the adjacent SnSe layers are stacked by weak van der Waals forces along the y-axis [28]. Therefore, SnSe can be expected to exfoliate along the [100] direction and exhibits a typical anisotropic layered structure [23]. High-resolution transmission electron microscopy (HRTEM) image shows clear orthogonal lattice fringes (Fig. 1(c)), with the lattice spacing along both the armchair and zigzag directions being about 0.3 nm, which matches well with published values [22]. The intersection angle between the (011) and ($0\bar{1}1$) planes in Fig. 1(c) is approximately 92°, which is consistent with a previous report [25]. Furthermore, an *ab initio* calculation of the band structure of bulk SnSe (Fig. 1(d)) shows an indirect band gap of 0.86 eV, with the valence-band maximum along Γ–Z, while the conduction-band minimum is along Γ–Y, in good agreement with previous reports [23, 24, 28].

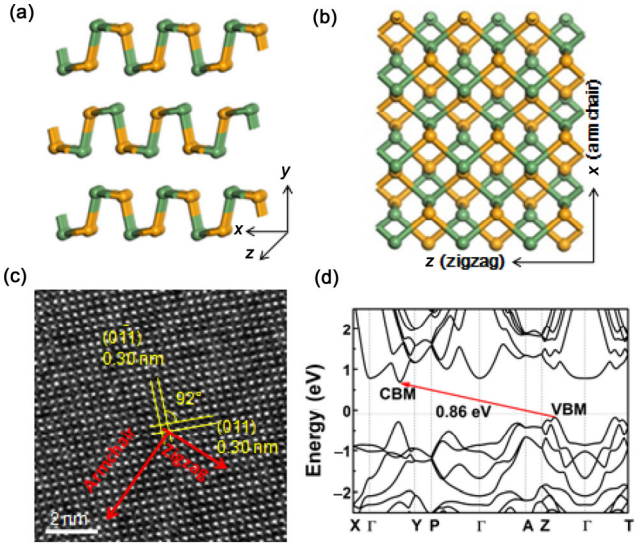

Figure 1 Schematics of the side view (a) and top view (b) of the multilayer SnSe flake structure, demonstrating its highly anisotropic nature. The green and yellow color represent Sn and Se atoms, respectively. (c) Typical HRTEM image of a SnSe flake. The armchair and zigzag directions are highlighted using red lines. (d) The calculated band structure of bulk SnSe flake based on DFT, with an indirect bandgap around 0.86 eV.

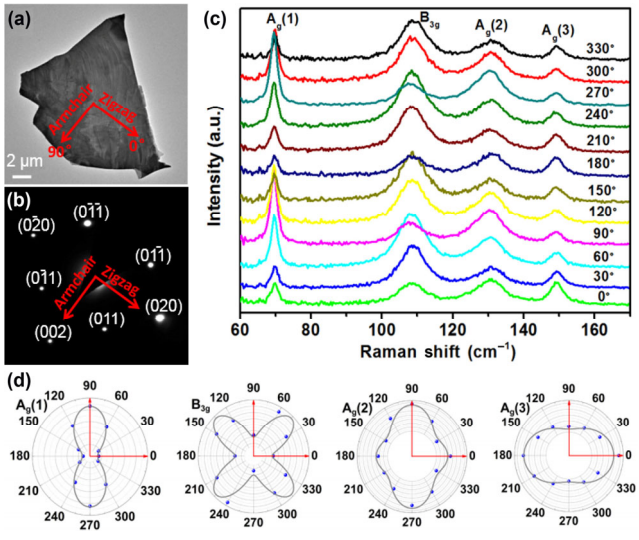

Figure 2 TEM image (a) and the corresponding SAED pattern (b) of a multilayer SnSe flake on the TEM grid. (c) The angle-resolved polarized Raman spectra of multilayer SnSe in (a). Here, 0° corresponds to the zigzag direction and 90° is the armchair direction. The sample in the *xz* plane is rotated to an angle θ between the incident polarization and the direction normal to the sample plane (from 0° to 360° with a step size of 30°). The excitation laser wavelength is 633 nm, and the power is around 0.5 mW. (d) The polar plots of Raman intensity with various polarization angles for four typical Raman modes. The blue dots and grey curves are the experimental values and fitted theory from Eqs. (1) and (2), respectively.

To examine the unique anisotropic nature of SnSe, we first investigated the in-plane anisotropic phonon behavior of a SnSe flake (with a thickness ~ 200 nm) on TEM grid, using angle-resolved polarized Raman spectra together with the corresponding TEM image and SAED. The detailed preparation of the TEM sample is described in the Experimental section. Based on TEM and SAED measurements (Figs. 2(a) and 2(b)), the zigzag direction of the crystalline orientation is identified and thereafter defined as the 0° angle. Figure 2(c) shows the polarized Raman spectra for different rotation angles, with four typical Raman peaks at 69.5, 109.0, 130.6, and 149.5 cm^{-1} clearly resolved, corresponding to the $A_g(1)$, B_{3g}, $A_g(2)$ and $A_g(3)$ modes, respectively [22, 31]. The Raman peak intensities show a clear dependence on the polarization; however, no obvious peak position shift is observed related to the polarization angle.

The polarization-dependent Raman intensities were analyzed and correlated with the crystallographic orientation. The polar plots of the Raman peak intensities as functions of the angle θ for typical A_g and B_g modes show highly distinct polarization dependence. The in-plane $A_g(1)$ and $A_g(2)$ modes show a strong correlation with the incident light polarization angles, having a period of 180° in its anisotropy with the maximum intensities along the 90° and 270° directions (armchair directions). The $A_g(3)$ mode shows a weaker anisotropy and the maximum Raman intensity turns towards the 0° or 180° directions (zigzag directions). Having a different symmetry from the A_g modes, the B_{3g} mode exhibits a 4-fold anisotropy with a period of 90°, with the minimum intensities along the 0° and 90° directions (the zigzag and armchair directions).

The anisotropic Raman phenomena in SnSe are strongly dependent on the phonon symmetry, similar to other 2D materials with in-plane anisotropy [7, 13, 14, 17]. The calculated band structure and symmetry of monolayer, double-layer, three-layer and bulk SnSe are shown in S1 in the Electronic Supplementary Material (ESM). It is obvious that the symmetry group of bulk SnSe is the largest, and the others are subgroups (Table S1 in the ESM). Odd and even layered SnSe

have different symmetry, in fact $\Gamma_{\text{Bulk}} = \Gamma_{\text{even}} \otimes \Gamma_{\text{odd}}$. Therefore, the phonon symmetries of SnSe with various thickness are different, as shown by this calculation.

We also explored the dependence of anisotropic Raman intensities on layer thickness-in the SnSe flakes. SnSe flakes with different thicknesses were prepared by micromechanical exfoliation from a SnSe single crystal synthesized by the Bridgman crystal growth technique [23]. We analyzed the anisotropic Raman intensities for three different thicknesses (71, 200, and 300 nm) with 488 and 633 nm laser excitation. Thinner samples were not included because of insufficient Raman signals. The polar plots of the polarized Raman intensities for the four typical A_g and B_g modes are shown in Table 1. It is apparent that sample thickness is important, in addition to phonon symmetry, in determining the anisotropy of Raman intensities. Here, the zigzag direction corresponds to the start of the sample rotation (0°). We note that, first, the minimum intensities of B_{3g} modes are always observed along the 0° and 90° directions for all thicknesses and excitation wavelengths, indicating that these two directions correspond to the zigzag and armchair directions of SnSe flakes, respectively. Under a given excitation wavelength, the direction of maximum intensity of the $A_g(1)$ and $A_g(2)$ modes changes between the armchair and zigzag directions with varying sample thickness. For example, both the $A_g(1)$ and $A_g(2)$ modes for the 71 nm-thick sample show the maximum intensity in the directions of 0° or 180° under excitation by 633 nm light . Interestingly, the $A_g(2)$ mode also shows secondary maxima at 90° and 270°. In contrast, in the 200 nm sample, the maximum intensities of the $A_g(1)$ and $A_g(2)$ modes change to the 90° and 270° directions. For the 300 nm sample, the polarized intensities of the $A_g(1)$ and $A_g(2)$ modes are largest at 90° and 270°, similar to the 200 nm sample. However, for the $A_g(3)$ mode, the polar plots change from weakly anisotropic to a pattern with maximum intensities at 0° and 180° as the sample thickness increases from 71 to 300 nm. A similar layer thickness-dependent switch of the main axes of the A_g modes between the armchair and zigzag directions has been reported in other studies of layered materials (e.g., black phosphorus) [13, 17]. Our Raman studies with a different excitation laser (488 nm) show that the excitation wavelength does not have an obvious impact on the observed anisotropic Raman properties in SnSe flakes.

To analyze the data (blue dots) shown in Table 1, we define the Raman tensor for the scattering process as $\boldsymbol{R}$. The Raman tensors of the A_g and B_g modes are therefore

$$\tilde{\boldsymbol{R}}_{A_g} = \begin{pmatrix} a & 0 & 0 \\ 0 & b & 0 \\ 0 & 0 & c \end{pmatrix} \qquad \tilde{\boldsymbol{R}}_{B_g} = \begin{pmatrix} 0 & 0 & 0 \\ 0 & 0 & g \\ 0 & g & 0 \end{pmatrix}$$

Where a, b, c, and g are the Raman tensor elements. When the polarization of the incident laser beam is rotated by θ with respect to the zigzag direction, the corresponding Raman intensity I varies with θ (for the parallel excitation/observation configuration used here) as [5, 17]:
for the A_g mode,

$$\begin{aligned} I^{\parallel}_{Ag} &= \left|(\sin\theta, 0, \cos\theta)\,\tilde{\boldsymbol{R}}\,(\sin\theta, \boldsymbol{0}, \cos\theta)^{\mathrm{T}}\right|^2 \\ &= \left(|a|\sin^2\theta + |c|\cos\varphi_{ca}\cos^2\theta\right)^2 + |c|^2\sin^2\varphi_{ca}\cos^4\theta \end{aligned} \tag{1}$$

for the B_{3g} mode,

$$I^{\parallel}_{B_{3g}} = |g|\sin^2\theta \tag{2}$$

where φ_{ca} is the phase difference between the Raman tensor elements c and a. Notice that the angular dependencies of the A_g(1 or 2) and the B_{3g} modes in the parallel configuration are well-fitted by Eqs. (1) and (2), respectively. According to the results (grey curves) of fitting the data in Table 1, the conventional approach, which considers only the Raman tensor, is applicable to the angular dependence of B_{3g} modes, while the new Raman approach outlined here, which combines the Raman tensor elements R with the phase difference φ_{ca}, can well explain the behaviors of the symmetric $A_g(1)$ and $A_g(2)$ modes [10]. However, the Raman tensor theory does not satisfactorily explain the polarization dependence of Raman intensities for all the A_g modes. Actually, the main axis directions of phonon modes with the same symmetry should be identical for excitation by the same wavelength. However, as seen in Table 1, the main axis directions of the $A_g(3)$ mode are at 0° and 180° for the 200 and

Table 1 Anisotropic Raman scattering from SnSe flakes with various thicknesses, under different incident laser wavelengths

Mode	$A_g(1)$	B_{3g}	$A_g(2)$	$A_g(3)$
(~71 nm) 633 nm excitation	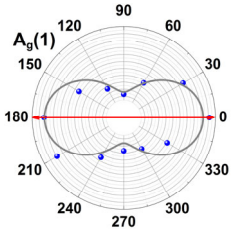	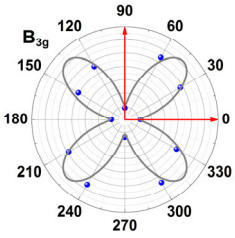	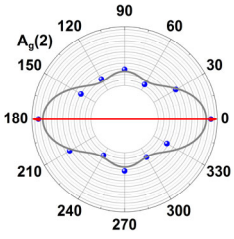	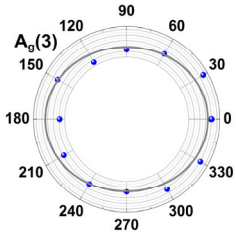
(~200 nm) 633 nm excitation	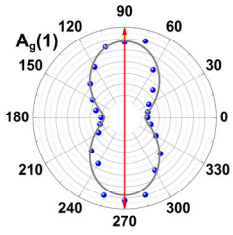	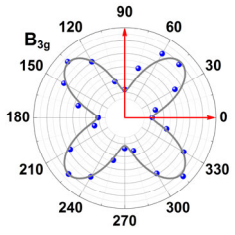	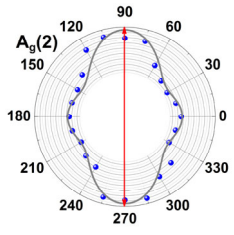	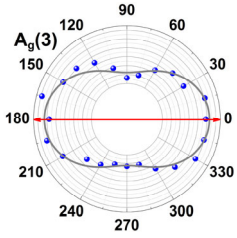
(~300 nm) 633 nm excitation	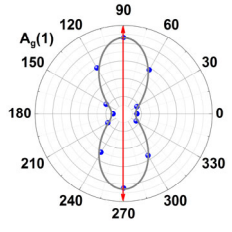	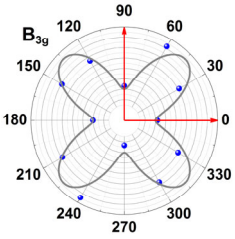	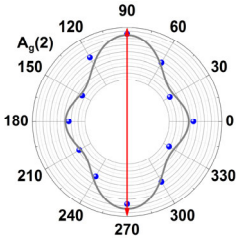	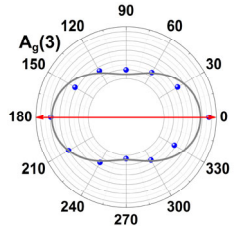
(~71 nm) 488 nm excitation	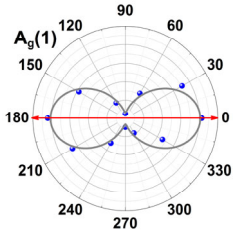	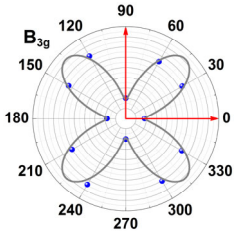	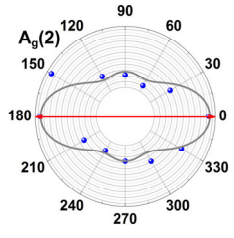	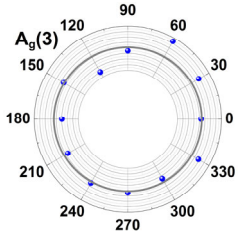
(~200 nm) 488 nm excitation	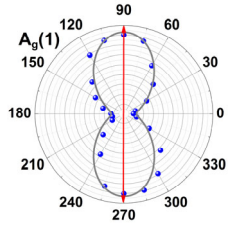	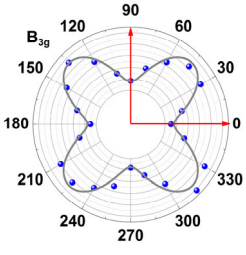	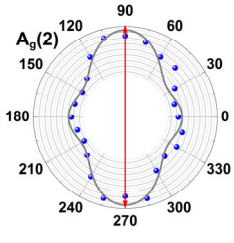	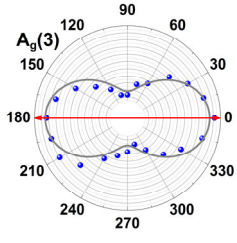
(~300 nm) 488 nm excitation	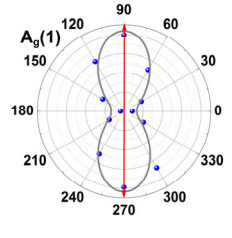	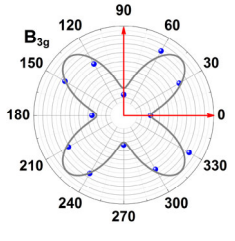	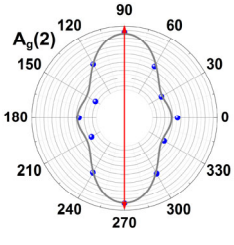	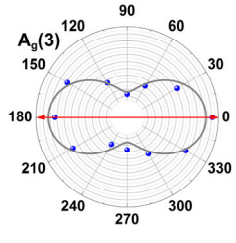

300 nm samples, which are perpendicular to those of the $A_g(1)$ and $A_g(2)$ modes. Therefore, additional detail in the theoretical analyses is necessary to explain the anisotropy of Raman intensities.

We then carry out the theoretical calculations on the Raman scattering process, involving the electron–photon and electron–phonon interactions. S2 in the ESM shows the detailed optical transition selection rules. We will take the transition processes of A_g and B_g modes in bulk SnSe as an example, which is shown in Fig. 3. Both transitions, from the A_g state to the B_u state and from the A_u state to the B_g state, occur under *X*-polarized light, while the transitions A_g to A_u and B_g to B_u occur with *Y*-polarization. Near the bandgap energy (E_g = 0.86 eV), the absorption for *Y*-polarized light is larger than for *X*-polarization, which is consistent with the experimental results in Table 1. For *Y* polarized light, the strongest transition happens at the valence band maximum (VBM) situated on the vector line Γ–Y (armchair direction), while for *X* polarized light, the strongest transition is along Γ–X (zigzag direction) (Fig. 3(a)). Therefore, for the A_g mode, as it does not involve a change of symmetry in the intermediate states, the Raman scattering may have non-zero values along both the armchair and zigzag directions. The specific shape of the polar diagram depends on the transition matrix. The possible shapes of the polar diagram for A_g-mode Raman scattering are shown in Figs. 3(b)–3(e). Obviously, the electron-phonon interaction shown in Fig. S3 (in the ESM) is anisotropic, giving a 180° period in the polarization dependence of Raman intensities. As shown in Figs. 3(b) and 3(d), the polar diagram of the A_g-mode Raman scattering mainly arises from *Y*-polarized light, similar to the data in Table 1 for the $A_g(1)$ and $A_g(2)$ modes in the 200 and 300 nm samples. Therefore, the main axes of the $A_g(1)$ and $A_g(2)$ modes are along the armchair direction. Since the $A_g(3)$ mode has the shape shown in Fig. 3(c), *X*-polarized light dominates in the absorption, and its main axis is along the zigzag direction. For the B_{3g} mode, which involves a change in symmetry in the intermediate states, the final state will differ from the initial state if the polarized direction of the light does not change (see Tables S2 and S3 in the ESM). Therefore, the Raman scattering polar diagram may have the shape in Fig. 3(f) with a period of 90° in the polarization dependence.

Besides its unique structure and Raman anisotropy, we have also studied the anisotropic electrical properties of few-layer SnSe FETs through angle-resolved

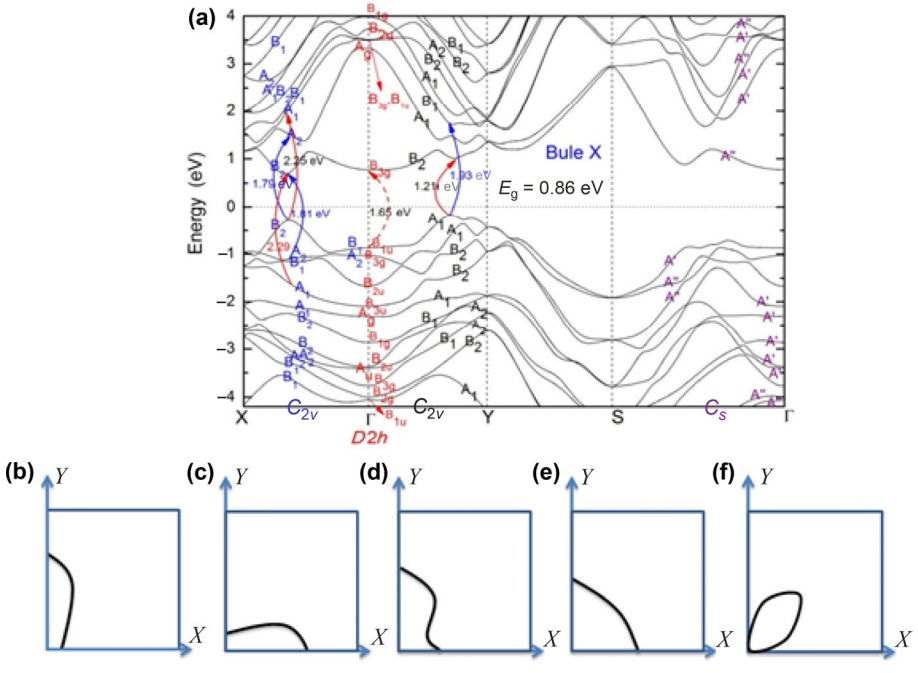

Figure 3 (a) Possible optical transition selection rules in bulk SnSe. (b)–(e) Possible shapes of the Raman-scattering polar plots for A_g modes. (f) Possible shape of the Raman-scattering polar plots for the B_{3g} mode.

transport measurements and related theoretical calculations. All electrical transport studies were carried out in vacuum at room temperature. To fabricate the devices, few-layer SnSe flakes (~ 10 nm) were first mechanically exfoliated onto a SiO_2/p^{++} Si substrate with 300 nm-thick SiO_2 as the back-gate dielectric. Next, Ni/Au (20/50 nm) metal contacts were symmetrically positioned around the SnSe flake, spaced at angles 45° apart along the directions shown in the inset of Fig. 4(a). We used the four pairs of diametrically-opposite bars as source/drain contacts for a transistor geometry and measured the transport behavior for each of these devices by applying an electrical field (the back-gate voltage V_{bg} was in the range −40 to + 60 V). In general, the conductance of few-layer SnSe transistors increases with higher positive V_{bg}, revealing a typical n-type behavior. The field-effect mobility can be extracted using the equation $\mu_x = [dI_{ds}/dV_{bg}] \times [L/(WC_iV_{ds})]$, where I_{ds} and V_{ds} are the source-drain current and voltage, C_i = 1.15 × 10^{-4} F·m^{-2} is the capacitance per unit area between the conducting channel and the back gate ($C_i = \varepsilon_0\varepsilon_r/d$); the relative dielectric constant ε_r of the SiO_2 insulating layer is 3.9 and thickness d is 300 nm; L and W are the length and width of the channel, respectively. The normalized field-effect mobility along the eight directions is highly angle-dependent, as seen in the polar coordinate plot (blue dots in Fig. 4(b)). The largest mobility occurs in the 30° (210°) direction, while the lowest is at 120° (300°). This angle-resolved mobility values can be closely fitted by the equation [21]

$$\mu_\theta = \mu_x \cos^2(\theta - \phi) + \mu_z \sin^2(\theta - \phi) \quad (3)$$

where μ_x and μ_z refer to the mobility of few-layer SnSe along the x- and z-axes, respectively; θ is an

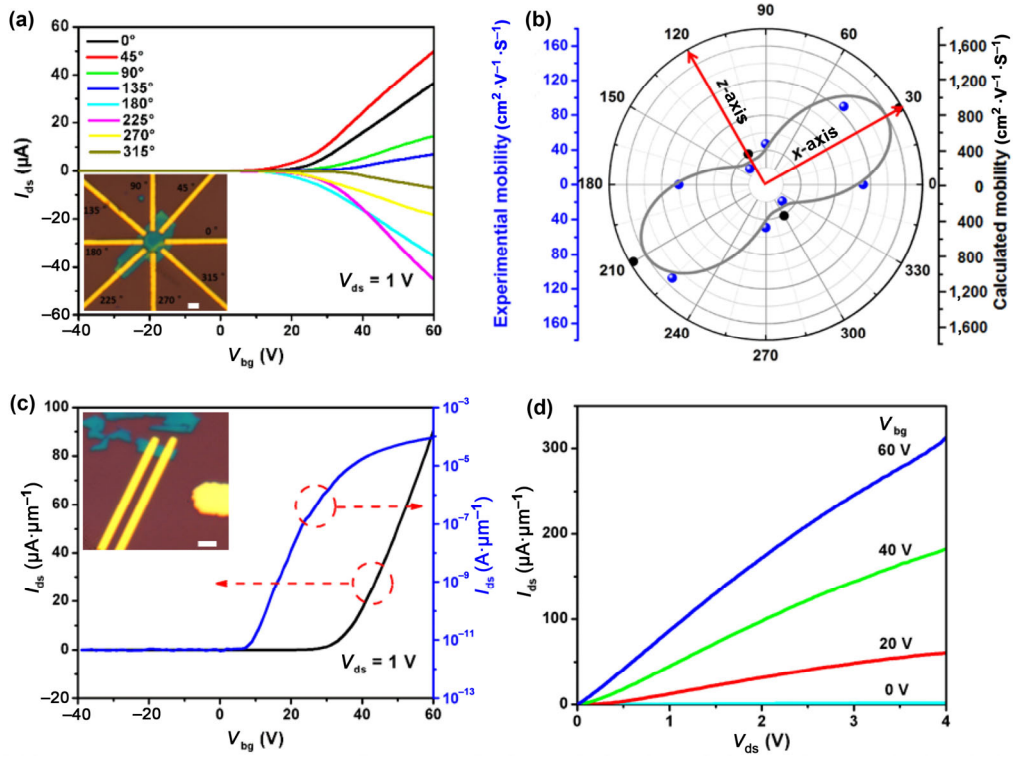

Figure 4 (a) Room-temperature I_{ds}–V_{bg} transfer curves of anisotropic few-layer SnSe transistors under 1 V drain-source bias voltage. Inset shows the optical image of the device with 8 electrodes spaced 45° apart. The scale bar is 2 μm. (b) Normalized maximum field-effect mobility of the SnSe transistor (shown in (a)) along 8 directions plotted in polar coordinates (blue dots correspond to the left axis scale). The grey line shows the fitted curve. The calculated mobility of bulk SnSe along two orientations (x- and z-axis) is plotted in the same graph (black dots – right axis) for comparison. The direction with the lowest mobility was designated 120° (or 300°) for reference. (c) Room-temperature I_{ds}–V_{bg} transfer characteristics of the best SnSe transistors along the x-direction. The drain-source bias voltage V_{ds} is set to 1 V. Inset is an optical image of the device with a scale bar of 4 μm. (d) Output characteristics of few-layer SnSe transistors with various back-gate voltages V_{bg} (0 to 60 V, 20 V step).

angle with respect to the 0° reference; μ_θ is the mobility along the θ direction, and ϕ is the angle between the x-axis and the 0° reference. The anisotropic ratio of mobility along the x- and z-axes (μ_{max}/μ_{min}) is ~ 5.8 for the few-layer SnSe flake. To the best of our knowledge, this ratio represents the highest reported for 2D anisotropic materials (compared to 3.1 for ReS_2 flake [1] and 1.5 for thin-layer BP [21]). To fully understand such a high electrical anisotropy ratio, we calculated the effective mass and mobility of few-layer SnSe along two crystalline orientations (x- and z-directions) using an *ab initio* method (see S3 and S4 in the ESM); the results are plotted in Fig. 4(b) (black dots, referring to the right-side scale). The theoretical calculation offers a qualitative explanation for the angular dependence of the experimental mobility, where the x-axis (defined as 30° or 210°) presents the largest mobility and the z-axis (defined as 120° or 300°) has the lowest. The anisotropic ratio of mobility μ_x/μ_z found by the theoretical calculation is ~ 4.3, slightly smaller than the experimental value.

To further probe the electrical performance limit, over 20 SnSe transistors with two terminal configurations were fabricated. The best electrical results and the device optical image are shown in Figs. 4(c) and 4(d), with the highest FET mobility being 254 $cm^2 \cdot V^{-1} \cdot s^{-1}$, an ON current density 0.3 $mA \cdot \mu m^{-1}$, and an ON–OFF ratio exceeding ~ 2×10^7. We note that the mobility and current density of the SnSe device are comparable to back-gate FETs of BP thin film without a top dielectric coupling, but the SnSe ON–OFF ratio is much higher [32]. In addition, our SnSe device is much more stable when exposed to air for 3 months, while displaying a similar electrical performance to the original device. Overall, 2D SnSe has been demonstrated to be a promising material for the next generation of high mobility, air-stable electronic devices.

Polarized optical absorption is also a simple method to identify the crystalline orientation in 2D anisotropic materials [13, 17, 33]. We measured the angle-resolved optical absorption spectra of multilayer SnSe (with a thickness ~ 200 nm) on a quartz substrate with wavelengths ranging from 450 to 750 nm. As in the polarized Raman studies, the zigzag and armchair orientations are defined as the 0° and 90° directions. An optical image of the device studied is shown in the inset of Fig. 5(a). A white light beam, passed through a polarizer, was used as the excitation source. The absorbance (A) plotted here is calculated simply as $A = \ln(I_0/I)$, where I_0 and I are the transmitted light intensities after the beam has passed through the quartz substrate and the multilayer SnSe, respectively [13, 17]. From the angle-dependent optical absorption spectra (Fig. 5(a)), the multilayer SnSe shows anisotropic light absorption, with the absorption of light polarized in the 90° direction (the armchair direction) being higher than at 0° (the zig-zag direction). In Fig. 5(b) the polar plots of the absorbance at 660 nm (1.88 eV)

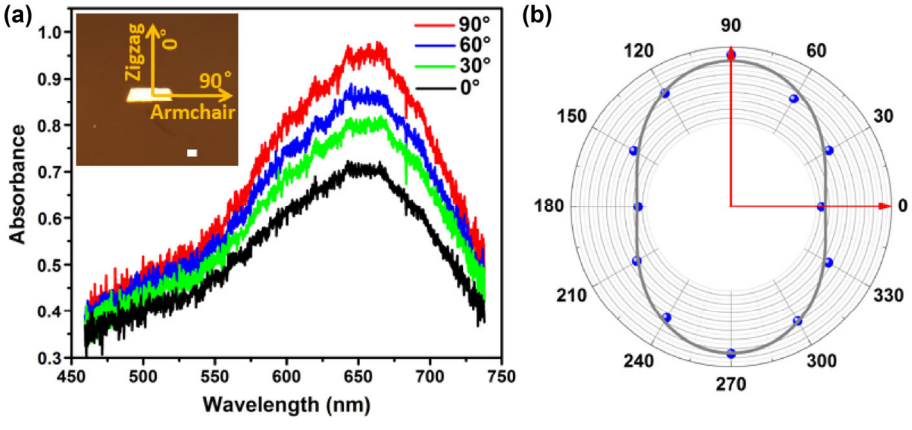

Figure 5 (a) Typical anisotropic absorption spectra of a multilayer SnSe flake with various polarization angles. Inset: optical image of the measured SnSe flake. The scale bar is 2 μm. (b) The corresponding polar plots of the absorbance at 660 nm (1.88 eV) versus the sample rotation angle in a plane normal to the flake. The symbols are the experimental values, and the lines are least-squares fittings. 0° and 90° correspond to the zigzag and armchair directions, respectively.

as a function of polarization angle further confirm the anisotropic characteristics of multilayer SnSe flake.

4 Conclusions

In conclusion, we have reported the angle-resolved Raman scattering, optical absorption, and electrical transport characteristics of layered SnSe, revealing its in-plane anisotropic nature. The relation of the Raman mode intensities to the crystalline orientations in layered SnSe is highly dependent on the sample thickness, which can be explained by the optical transition selection rules. Optical absorption is anisotropic, being stronger for polarization along the armchair direction. Few-layer SnSe FETs show excellent performance with a large current ON–OFF ratio (~ 2×10^7) and the highest anisotropic ratio of mobility (~ 5.8) reported among 2D anisotropic materials. SnSe crystal also exhibits strongly anisotropic thermoelectric properties, although these are not addressed in this report. The polarized optical spectra and direction-sensitive transport measurements offer a simple and convenient way to identify crystalline orientation, which is beneficial for the future exploration of the anisotropic nature of layered SnSe and other low-symmetry 2D materials. In addition, our study enables the fabrication of electronic devices with performance controlled through choice of crystalline direction. Layered SnSe shows promise for the integration of anisotropic optics, electronics, optoelectronics, and thermionics in high-performance devices.

Acknowledgements

We thank the support from National Science Foundation through the grant DMR1508144. S. X. Y. is supported by the National Natural Science Foundation of China (No. 51602014) and Fundamental Research Funds for the Central Universities (No. YWF-17-BJ-Y-112). C. B. J. is supported by the National Natural Science Foundations of China (No. 51331001). S. H. W. is supported by the National Natural Science Foundations of China (No. 51672023). We thank Prof. Dehui Li for discussing the experiments and related data.

Electronic Supplementary Material: Supplementary material (band structure, the optical transition selection rules, and mobility calculation) is available in the online version of this article at https://doi.org/10.1007/s12274-017-1712-2.

References

[1] Liu, E. F.; Fu, Y. J.; Wang, Y. J.; Feng, Y. Q.; Liu, H. M.; Wan, X. G.; Zhou, W.; Wang, B. G.; Shao, L. B.; Ho, C. H. et al. Integrated digital inverters based on two-dimensional anisotropic ReS_2 field-effect transistors. *Nat. Commun.* **2014**, *6*, 6991.

[2] Qiao, X. F.; Wu, J. B.; Zhou, L. W.; Qiao, J. S.; Shi, W.; Chen, T.; Zhang, X.; Zhang, J.; Ji, W.; Tan, P. H. Polytypism and unexpected strong interlayer coupling in two-dimensional layered ReS_2. *Nanoscale* **2016**, *8*, 8324–8332.

[3] Tao, J.; Shen, W. F.; Wu, S.; Liu, L.; Feng, Z. H.; Wang, C.; Hu, C. G.; Yao, P.; Zhang, H.; Pang, W. et al. Mechanical and electrical anisotropy of few-layer black phosphorus. *ACS Nano* **2015**, *9*, 11362–11370.

[4] Chenet, D. A.; Aslan, O. B.; Huang, P. Y.; Fan, C.; van der Zande, A. M.; Heinz, T. F.; Hone, J. C. In-plane anisotropy in mono- and few-layer ReS_2 probed by Raman spectroscopy and scanning transmission electron microscopy. *Nano Lett.* **2015**, *15*, 5667–5672.

[5] Hart, L.; Dale, S.; Hoye, S.; Webb, J. L.; Wolverson, D. Rhenium dichalcogenides: Layered semiconductors with two vertical orientations. *Nano Lett.* **2016**, *16*, 1381–1386.

[6] Zhao, H.; Wu, J. B.; Zhong, H. X.; Guo, Q. S.; Wang, X. M.; Xia, F. N.; Yang, L.; Tan, P. H.; Wang, H. Interlayer interactions in anisotropic atomically thin rhenium diselenide. *Nano Res.* **2015**, *8*, 3651–3661.

[7] Hafeez, M.; Gan, L.; Li, H. Q.; Ma, Y.; Zhai, T. Y. Chemical vapor deposition synthesis of ultrathin hexagonal $ReSe_2$ flakes for anisotropic Raman property and optoelectronic application. *Adv. Mater.* **2016**, *28*, 8296–8301.

[8] Ali, M. N.; Xiong, J.; Flynn, S.; Tao, J.; Gibson, Q. D.; Schoop, L. M.; Liang, T.; Haldolaarachchige, N.; Hirschberger, M.; Ong, N. P. et al. Large, non-saturating magnetoresistance in WTe_2. *Nature* **2014**, *514*, 205–208.

[9] Wang, C.; Yang, S. X.; Xiong, W. Q.; Xia, C. X.; Cai, H.; Chen, B.; Wang, X. T.; Zhang, X. Z.; Wei, Z. M.; Tongay, S. et al. Gate-tunable diode-like current rectification and ambipolar transport in multilayer van der Waals $ReSe_2/WS_2$ p–n heterojunctions. *Phys. Chem. Chem. Phys.* **2016**, *18*, 27750–27753.

[10] Ribeiro, H. B.; Pimenta, M. A.; de Matos, C. J. S.; Moreira, R. L.; Rodin, A. S.; Zapata, J. D.; de Souza, E. A. T.; Neto, A. H. C. Unusual angular dependence of the Raman response

in black phosphorus. *ACS Nano* **2015**, *9*, 4270–4276.

[11] Zhao, L. D.; Tan, G. J.; Hao, S. Q.; He, J. Q.; Pei, Y. L.; Chi, H.; Wang, H.; Gong, S. K.; Xu, H. B.; Dravid, V. P. et al. Ultrahigh power factor and thermoelectric performance in hole-doped single-crystal SnSe. *Science* **2016**, *351*, 141–144.

[12] Safdar, M.; Wang, Q. S.; Mirza, M.; Wang, Z. X.; Xu, K.; He, J. Topological surface transport properties of single-crystalline SnTe nanowire. *Nano Lett*. **2013**, *13*, 5344–5349.

[13] Huang, S. X.; Tatsumi, Y.; Ling, X.; Guo, H. H.; Wang, Z. Q.; Watson, G.; Puretzky, A. A.; Geohegan, D. B.; Kong, J.; Li, J. et al. In-plane optical anisotropy of layered gallium telluride. *ACS Nano* **2016**, *10*, 8964–8972.

[14] Wu, J. X.; Mao, N. N.; Xie, L. M.; Xu, H.; Zhang, J. Identifying the crystalline orientation of black phosphorus using angle-resolved polarized Raman spectroscopy. *Angew. Chem., Int. Ed*. **2015**, *54*, 2366–2369.

[15] Wang, C.; Yang, S. X.; Cai, H.; Ataca, C.; Chen, H.; Zhang, X. Z.; Xu, J. J.; Chen, B.; Wu, K. D.; Zhang, H. R. et al. Enhancing light emission efficiency without color change in post-transition metal chalcogenides. *Nanoscale* **2016**, *8*, 5820–5825.

[16] Yang, S. X.; Wang, C.; Ataca, C.; Li, Y.; Chen, H.; Cai, H.; Suslu, A.; Grossman, J. C.; Jiang, C. B.; Liu, Q. et al. Self-driven photodetector and ambipolar transistor in atomically thin GaTe-MoS_2 p−n vdW heterostructure. *ACS Appl. Mater. Interfaces* **2016**, *8*, 2533−2539.

[17] Ling, X.; Huang, S. X.; Hasdeo, E. H.; Liang, L. B.; Parkin, W. M.; Tatsumi, Y.; Nugraha, A. R. T.; Puretzky, A. A.; Das, P. M.; Sumpter, B. G. et al. Anisotropic electron–photon and electron–phonon interactions in black phosphorus. *Nano Lett*. **2016**, *16*, 2260–2267.

[18] Tian, H.; Guo, Q. S.; Xie, Y. J.; Zhao, H.; Li, C.; Cha, J. J.; Xia, F. N.; Wang, H. Anisotropic black phosphorus synaptic device for neuromorphic applications. *Adv. Mater*. **2016**, *28*, 4991–4997.

[19] Xue, D. J.; Tan, J. H.; Hu, J. S.; Hu, W. P.; Guo, Y. G.; Wan, L. J. Anisotropic photoresponse properties of single micrometer-sized GeSe nanosheet. *Adv. Mater*. **2012**, *24*, 4528–4533.

[20] Ge, S. F.; Li, C. K.; Zhang, Z. M.; Zhang, C. L.; Zhang, Y. D.; Qiu, J.; Wang, Q. S.; Liu, J. K.; Jia, S.; Feng, J. et al. Dynamical evolution of anisotropic response in black phosphorus under ultrafast photoexcitation. *Nano Lett*. **2015**, *15*, 4650–4656.

[21] Xia, F. N.; Wang, H.; Jia, Y. C. Rediscovering black phosphorus as an anisotropic layered material for optoelectronics and electronics. *Nat. Commun*. **2014**, *5*, 4458.

[22] Zhao, S. L.; Wang, H.; Zhou, Y.; Liao, L.; Jiang, Y.; Yang, X.; Chen, G. C.; Lin, M.; Wang, Y.; Peng, H.L. et al. Controlled synthesis of single-crystal SnSe nanoplates. *Nano Res*. **2015**, *8*, 288–295.

[23] Zhao, L. D.; Lo, S. H.; Zhang, Y. S.; Sun, H.; Tan, G. J.; Uher, C.; Wolverton, C.; Dravid, V. P.; Kanatzidis, M. G. Ultralow thermal conductivity and high thermoelectric figure of merit in SnSe crystals. *Nature* **2014**, *508*, 373–377.

[24] Antunez, P. D.; Buckley, J. J.; Brutchey, R. L. Tin and germanium monochalcogenide IV–VI semiconductor nanocrystals for use in solar cells. *Nanoscale* **2011**, *3*, 2399–2411.

[25] Vaughn II, D. D.; In, S. I.; Schaak, R. E. A precursor-limited nanoparticle coalescence pathway for tuning the thickness of laterally-uniform colloidal nanosheets: The case of SnSe. *ACS Nano* **2011**, *5*, 8852–8860.

[26] Pejova, B.; Tanuševsk, A. A Study of photophysics, photoelectrical properties, and photoconductivity relaxation dynamics in the case of nanocrystalline Tin(II) selenide thin films. *J. Phys. Chem. C* **2008**, *112*, 3525–3537.

[27] Agarwal, A.; Vashi, M. N.; Lakshminarayana, D.; Batra, N. M. Electrical resistivity anisotropy in layered p-SnSe single crystals. *J. Mater. Sci. Mater. Electron*. **2000**, *11*, 67–71.

[28] Shi, G. S.; Kioupakis, E. Anisotropic spin transport and strong visible-light absorbance in few-layer SnSe and GeSe. *Nano Lett*. **2015**, *15*, 6926–6931.

[29] Li, L.; Chen, Z.; Hu, Y.; Wang, X. W.; Zhang, T.; Chen, W.; Wang, Q. B. Single-layer single-crystalline SnSe nanosheets. *J. Am. Chem. Soc*. **2013**, *135*, 1213–1216.

[30] Carrete, J.; Mingo, N.; Curtarolo, S. Low thermal conductivity and triaxial phononic anisotropy of SnSe. *Appl. Phys. Lett*. **2014**, *105*, 101907.

[31] Zhang, J.; Zhu, H. Y.; Wu, X. X.; Cui, H.; Li, D. M.; Jiang, J. R.; Gao, C. X.; Wang, Q. S.; Cui, Q. L. Plasma-assisted synthesis and pressure-induced structural transition of single-crystalline SnSe nanosheets. *Nanoscale* **2015**, *7*, 10807–10816.

[32] Das, S.; Demarteau, M.; Roelofs, A. Ambipolar phosphorene field effect transistor. *ACS Nano* **2014**, *8*, 11730–11738.

[33] Wu, J. B.; Zhao, H.; Li, Y. R.; Ohlberg, D.; Shi, W.; Wu, W.; Wang, H.; Tan, P. H. Monolayer molybdenum disulfide nanoribbons with high optical anisotropy. *Adv. Opt. Mater*. **2016**, *4*, 756–762.